

## A CHANDRA CATALOG OF X-RAY SOURCES IN THE CENTRAL 150 PC OF THE GALAXY

M. P. MUNO,<sup>1,2</sup> F. E. BAUER,<sup>3,4</sup> R. M. BANDYOPADHYAY,<sup>5,6</sup> AND Q. D. WANG<sup>7,8</sup>

*Draft version June 26, 2018*

### ABSTRACT

We present the catalog of X-ray sources detected in a shallow *Chandra* survey of the inner  $2^\circ \times 0.8^\circ$  of the Galaxy, and in two deeper observations of the Radio Arches and Sgr B2. The catalog contains 1352 objects that are highly-absorbed ( $N_{\text{H}} \gtrsim 4 \times 10^{22} \text{ cm}^{-2}$ ) and are therefore likely to lie near the Galactic center ( $D \approx 8 \text{ kpc}$ ), and 549 less-absorbed sources that lie within  $\lesssim 6 \text{ kpc}$  of Earth. Based on the inferred luminosities of the X-ray sources and the expected numbers of various classes of objects, we suggest that the sources with  $L_{\text{X}} \lesssim 10^{33} \text{ erg s}^{-1}$  that comprise  $\approx 90\%$  of the catalog are cataclysmic variables, and that the  $\approx 100$  brighter objects are accreting neutron stars and black holes, young isolated pulsars, and Wolf-Rayet and O stars in colliding-wind binaries. We find that the spatial distribution of X-ray sources matches that of the old stellar population observed in the infrared, which supports our suggestion that most of the X-ray sources are old cataclysmic variables. However, we find that there is an apparent excess of  $\approx 10$  bright sources in the Radio Arches region. That region is already known to be the site of recent star formation, so we suggest that the bright sources in this region are young high-mass X-ray binaries, pulsars, or WR/O star binaries. We briefly discuss some astrophysical questions that this catalog can be used to address.

*Subject headings:* catalogs — Galaxy: center — X-rays: general

### 1. INTRODUCTION

The exquisite sensitivity of the *Chandra X-ray Observatory* has provided vast improvements in our understanding of faint, hard X-ray sources. *Chandra* observations of distant galaxies allow us to study the X-ray population at luminosities similar to those accessible in our own Galaxy with wide-field X-ray instruments like the *Rossi X-ray Timing Explorer* All-Sky Monitor and the *BeppoSAX* Wide-Field Camera ( $L_{\text{X}} \sim 10^{36} \text{ erg s}^{-1}$ ), while observations of our own Galaxy are sensitive to sources a million times fainter than found with previous wide-field surveys. One of the most dramatic products of this improvement in sensitivity are the *Chandra* observations of the Galactic center (Wang, Gotthelf, & Lang 2002; Baganoff et al. 2003). Whereas previous imaging surveys identified dozens of X-ray sources against a background of bright Galactic diffuse emission (Watson et al. 1981; Pavlinsky, Grebenev, & Sunyaev 1994; Predehl & Truemper 1995; Sidoli et al. 2001, 1999; Sakano et al. 2002), *Chandra* observations have revealed thousands of individual X-ray sources (e.g., Wang et al. 2002; Munro et al. 2003) and discrete, filamentary features (e.g., Lu, Wang, & Lang 2003; Yusef-Zadeh et al. 2005a). This high concentration of X-ray sources is not surprising. The  $2^\circ \times 0.8^\circ$  ( $300 \times 125 \text{ pc}$  for a distance of

8 kpc; McNamara et al. 2000) region centered on the Galactic center contains roughly 1% of the Galactic mass (Lauhardt, Zylka, & Mezger 2002). Moreover, unlike the Galactic bulge, star formation has occurred continuously in the central region of the Galaxy, as is strikingly illustrated by the  $\gtrsim 60$  ultra-compact HII regions in the giant molecular cloud Sgr B2 (de Pree, Goss, & Gaume 1998), and by three young, dense clusters of massive stars (the Arches, the Quintuplet, and the Central Parsec; Krabbe et al. 1995; Figer et al. 1999).

A wealth of questions can be addressed with *Chandra* observations, and with subsequent comparisons to multi-wavelength catalogs. For instance, a variety of studies of the synthesis of compact, accreting binaries have been designed to explain the large number of X-ray sources *Chandra* detects in the Galactic center, and the results constrain, for example, the amount of angular momentum dissipated in the common envelope phase (e.g., Pfahl, Rappaport, & Podsiadlowski 2002; Belczynski & Taam 2004; Liu & Li 2005; Ruiter, Belczynski, & Harrison 2005). *Chandra* also can detect outbursts from transient low-mass X-ray binaries (LMXBs) at much lower flux levels than are accessible with traditional wide-field X-ray surveys, which provides unique insight into the duty cycles and emission mechanisms of compact objects accreting at very low rates ( $\dot{M} \lesssim 10^{-11} M_{\odot} \text{ yr}^{-1}$ ; e.g., King 2000; Wijnands, Miller, & Wang 2002; Wijnands & Wang 2002; in't Zand 2005; Sakano et al. 2005). Combining *Chandra* and radio observations can be used to identify young stars with powerful winds, which helps to constrain the rate at which massive stars have formed recently in the Galactic center (Yusef-Zadeh et al. 2002; Law & Yusef-Zadeh 2004; Munro et al. 2005b).

Several observational studies have discussed the population of X-ray sources in *Chandra* surveys of the Galactic center. Wang et al. (2002) presented images from shallow (12 ks) *Chandra* exposures of the  $2^\circ \times 0.8^\circ$  around

<sup>1</sup> Department of Physics and Astronomy, University of California, Los Angeles, CA 90095; mmuno@astro.ucla.edu

<sup>2</sup> Hubble Fellow

<sup>3</sup> Columbia Astrophysics Laboratory, Columbia University, Pupin Laboratories, 550 W. 120th St., Rm 1418, NY, NY, 10027

<sup>4</sup> Chandra Fellow

<sup>5</sup> Dept. of Astrophysics, University of Oxford, Keble Road, Oxford OX1 3RH, U.K.

<sup>6</sup> Dept. of Astronomy, University of Florida, 211 Bryant Space Science Center, Gainesville, FL, 32611 USA

<sup>7</sup> Department of Astronomy, University of Massachusetts, Amherst, MA 01003; wqd@astro.umass.edu

<sup>8</sup> Institute for Advanced Study, Einstein Drive, Princeton, NJ 08540



FIG. 1.— Mosaic image of the  $0.8 \times 2^\circ$  field along the Galactic plane, centered on Sgr A\*. The raw image has been adaptively smoothed with the CIAO tool `csmooth` for display purposes. The prominent features are the Sgr A complex at the center of the image, two bright X-ray binaries and their dust scattering halos at  $l=0.275^\circ$  and  $-0.88^\circ$ . Only a fraction of the brightest point sources are visible in this image. Note that the smoothing algorithm introduces significant artifacts, especially at the edges of the deep observations centered on Sgr B2 and the Arches.

Sgr A\*, and gave a general overview of the number of X-ray sources and the properties of the diffuse X-ray emission. Takagi, Murakami, & Koyama (2002) studied the properties of X-ray sources associated with HII regions in Sgr B2. Yusef-Zadeh et al. (2002) and Law & Yusef-Zadeh (2004) and studied the X-ray emission from massive stars in several clusters, including the Arches and Quintuplet. Finally, Muno et al. (2003, 2004b, 2005a), presented a comprehensive study of the population of X-ray sources with  $L_X = 10^{31} - 10^{33}$  erg  $s^{-1}$  that were discovered in a deep (625 ks) set of *Chandra* observations of the inner 25 pc around Sgr A\*. However, aside from the inner 25 pc, no catalog containing all of the X-ray sources found within the inner 150 pc of the Galactic center has been published.

In this paper, we rectify this by reporting the locations and basic properties of the X-ray sources detected in *Chandra* observations of the inner  $2^\circ \times 0.8^\circ$  around the Galactic center. In §2.1, we present the locations of these X-ray sources (excluding the inner  $8'$  covered by the catalog in Muno et al. 2003) in order to facilitate searches for multi-wavelength counterparts. In §2.2, we present the fluxes and basic spectral properties in order to constrain the origin of the X-ray emission, and to serve as baseline measurements for future searches for transient sources. In §3.1, we examine the spatial distribution of the X-ray sources to determine how they are related to the stellar population that is observed in the infrared. In §3.2, we study the luminosity distribution of the X-ray sources, and report variations in the relative numbers of bright sources that could be related to recent star formation.

## 2. OBSERVATIONS

The central  $300 \times 125$  pc of the Galaxy has been observed on several occasions with the imaging array of the *Chandra* Advanced CCD Imaging Spectrometer (ACIS-I Weisskopf et al. 2002). The entire region was surveyed with overlapping  $\approx 12$  ks observations (Wang et al. 2002),

and one additional short observation was obtained centered on the LMXB 1E 1740.7–2942. Deeper observations were taken of the HII regions in the giant molecular cloud Sgr B2 (100 ks; Takagi et al. 2002), and the non-thermal radio features referred to as the Arches (50 ks of public data as of 2005 June; Law & Yusef-Zadeh 2004). We list each of these observations in Table 1, and present a mosaic image of the survey in Figure 1.

The ACIS-I is a set of four 1024-by-1024 pixel CCDs, covering a field of view of  $17'$  by  $17'$ . When placed on-axis at the focal plane of the grazing-incidence X-ray mirrors, the imaging resolution is determined primarily by the pixel size of the CCDs,  $0''.492$ . The CCDs also measure the energies of incident photons within a calibrated energy band of 0.5–8 keV, with a resolution of 50–300 eV (depending on photon energy and distance from the read-out node). The CCD frames are read out every 3.2 s, which provides the nominal time resolution of the data.

We reduced the observations using standard tools from the CIAO package, version 2.3.01. We started with the level-1 event lists provided by the *Chandra* X-ray Center (CXC), and removed the pixel randomization applied by the default processing software. We then modified the pulse heights of each event to partially correct for the position-dependent charge-transfer inefficiency caused by radiation damage early in the mission, using software provided by Townsley et al. (2002b). We excluded most events flagged as possible background, but left in possible cosmic ray afterglows because in the version of the processing software that we used they were difficult to distinguish from genuine X-rays from the strong diffuse emission and numerous point sources in the field. We applied the standard ASCA grade filters to the events, as well as the good-time filters supplied by the CXC. Finally, we searched each observation for time intervals when the detector background flared to  $\geq 3\sigma$  above the

TABLE 1  
OBSERVATIONS OF THE CENTRAL  $2^\circ \times 0.8^\circ$  OF THE GALAXY

| Start Time<br>(UT)   | Sequence | Target         | Exposure<br>(ks) | Aim Point             |           | Roll<br>(degrees) |
|----------------------|----------|----------------|------------------|-----------------------|-----------|-------------------|
|                      |          |                |                  | RA<br>(degrees J2000) | DEC       |                   |
| 2000 Aug 30 16:59:32 | 658      | 1E 1740.7–2942 | 9.2              | 265.97583             | –29.75008 | 270.8             |
| 2000 Mar 29 09:44:36 | 944      | SGR B2         | 97.5             | 266.78034             | –28.44169 | 87.8              |
| 2000 Jul 07 19:05:19 | 945      | GC ARC         | 48.8             | 266.58192             | –28.87196 | 284.4             |
| 2001 Jul 19 10:01:48 | 2267     | GCS 20         | 8.7              | 266.17150             | –29.27337 | 283.8             |
| 2001 Jul 20 04:37:11 | 2268     | GCS 21         | 10.8             | 265.98136             | –29.17141 | 283.8             |
| 2001 Jul 16 02:15:50 | 2269     | GCS 1          | 10.5             | 267.05495             | –28.37576 | 283.8             |
| 2001 Jul 20 08:00:49 | 2270     | GCS 22         | 10.6             | 266.24512             | –29.54138 | 283.8             |
| 2001 Jul 16 05:35:55 | 2271     | GCS 2          | 10.4             | 266.86502             | –28.27455 | 283.8             |
| 2001 Jul 20 11:12:40 | 2272     | GCS 23         | 11.6             | 266.05423             | –29.43957 | 283.8             |
| 2001 Jul 18 00:48:28 | 2273     | GCS 10         | 11.2             | 266.70988             | –28.87565 | 283.8             |
| 2001 Jul 16 08:44:25 | 2274     | GCS 3          | 10.4             | 266.67662             | –28.17301 | 283.8             |
| 2001 Jul 20 14:41:10 | 2275     | GCS 24         | 11.6             | 265.86371             | –29.33729 | 283.8             |
| 2001 Jul 18 04:16:58 | 2276     | GCS 11         | 11.6             | 266.51970             | –28.77438 | 283.8             |
| 2001 Jul 16 11:52:55 | 2277     | GCS 4          | 10.4             | 266.94061             | –28.54231 | 283.8             |
| 2001 Jul 20 18:09:40 | 2278     | GCS 25         | 11.6             | 266.12769             | –29.70775 | 283.8             |
| 2001 Jul 18 07:45:28 | 2279     | GCS 12         | 11.6             | 266.33020             | –28.67281 | 283.8             |
| 2001 Jul 16 15:01:25 | 2280     | GCS 5          | 10.4             | 266.75037             | –28.44124 | 283.8             |
| 2001 Jul 20 21:38:10 | 2281     | GCS 26         | 11.6             | 265.93652             | –29.60557 | 283.8             |
| 2001 Jul 18 11:13:58 | 2282     | GCS 13         | 10.6             | 266.59425             | –29.04216 | 283.8             |
| 2001 Jul 21 01:06:39 | 2283     | GCS 27         | 11.6             | 265.74584             | –29.50315 | 283.8             |
| 2001 Jul 18 14:25:48 | 2284     | GCS 14         | 10.6             | 266.40487             | –28.94088 | 283.8             |
| 2001 Jul 16 18:09:55 | 2285     | GCS 6          | 10.4             | 266.56112             | –28.34029 | 283.4             |
| 2001 Jul 21 04:35:09 | 2286     | GCS 28         | 11.6             | 266.00997             | –29.87372 | 283.8             |
| 2001 Jul 18 17:37:38 | 2287     | GCS 15         | 10.6             | 266.21439             | –28.83925 | 283.8             |
| 2001 Jul 17 14:11:51 | 2288     | GCS 7          | 11.1             | 266.82518             | –28.70891 | 283.8             |
| 2001 Jul 21 08:03:39 | 2289     | GCS 29         | 11.6             | 265.81855             | –29.77165 | 283.8             |
| 2001 Jul 21 11:32:10 | 2290     | GCS 30         | 11.6             | 265.62772             | –29.66900 | 283.8             |
| 2001 Jul 18 20:49:28 | 2291     | GCS 16         | 10.6             | 266.47839             | –29.20880 | 283.8             |
| 2001 Jul 17 17:51:28 | 2292     | GCS 8          | 11.6             | 266.63516             | –28.60795 | 283.8             |
| 2001 Jul 19 00:01:18 | 2293     | GCS 17         | 11.1             | 266.28794             | –29.10740 | 283.8             |
| 2001 Jul 17 21:19:58 | 2294     | GCS 9          | 11.6             | 266.44581             | –28.50671 | 283.8             |
| 2001 Jul 19 03:21:28 | 2295     | GCS 18         | 11.1             | 266.09836             | –29.00518 | 283.8             |
| 2001 Jul 19 06:41:38 | 2296     | GCS 19         | 11.1             | 266.36205             | –29.37522 | 283.8             |

mean level, and removed such intervals when they occurred (in ObsIDs 2267, 2269, 2273, 2288, and 944).

### 2.1. Source Detection and Initial Localization

We searched for X-ray sources separately in sets of 9 images for each observation using the wavelet routine `wavdetect` (Freeman et al. 2002). We generated images in three energy bands: the full 0.5–8.0 keV band, the 0.5–2.0 keV band to increase our sensitivity to foreground sources, and 4–8 keV to increase our sensitivity to highly absorbed sources. For the purposes of source detection only, we removed events that had been flagged as possible cosmic ray afterglows. We employed the default “Mexican Hat” wavelet, and used a sensitivity threshold of  $10^{-7}$  that corresponds to chance of detecting a spurious source per pixel if the local background is spatially uniform. We searched each energy band using a succession of three images centered on the aim point of each exposure:  $1024 \times 1024$  images at the full *Chandra* resolution of  $0''.5$ ,  $1024 \times 1024$  images binned by a factor of 2 to a resolution of  $1''$ , and images of variable size that covered the entire ACIS-I exposure for each observation with a resolution of  $2''$ . We used wavelet scales that increased by a factor of  $\sqrt{2}$ : 1–4 for the  $0''.5$  image, 1–8 for the  $1''$  image, and 1–16 for the  $2''$  image. This succession of three images and spatial scales were chosen because the

point-spread function (PSF) broadens as a function of offset from the aim point. The resulting source list from the 33 observations contained 1901 unique sources, 225 of which were only detected in the soft band, and 382 of which were only detected in the hard band. Based on the sensitivity threshold for `wavdetect` ( $10^{-7}$ ), we expect 2 spurious sources per field, or  $\sim 70$  in the entire survey.

We attempted to refine the astrometry for each observation by matching foreground X-ray sources detected in the soft band, many of which are likely to be K and M dwarf stars (Muno et al. 2003), to infrared sources in the Two-Micron All-Sky Survey (2MASS) catalog. For the two observations longer than 50 ks (Sgr B2 and the Arches), we found that there were  $\approx 20$  matches between the soft X-ray and 2MASS catalog within  $5'$  of the aim point. By randomly shifting the relative positions of the two catalogs, we determined that, with 90% confidence, fewer than 25% of these matches should be random. Based on these matches, we could derive the absolute astrometry of the *Chandra* pointing to within  $0''.1$ .

Unfortunately, the shorter observations were less sensitive, and contained far fewer X-ray sources. Whereas the  $\gtrsim 50$  ks exposures contained  $\approx 200$  X-ray sources, the shorter exposures generally contained only a couple dozen. In general,  $\leq 2$  X-ray sources could be iden-

tified with 2MASS counterparts, which was insufficient to improve the pipeline astrometry. Therefore, starting with the fields adjacent to the deep exposures of Sgr A\* (Muno et al. 2003), the Arches, and Sgr B2 and moving outward, we derived the astrometry by matching the `wavdetect` positions of the X-ray sources matched those of adjacent fields. Unfortunately, because most of the matches made in this way relied on X-ray sources detected  $\gtrsim 6'$  off-axis, the statistical uncertainty on the `wavdetect` positions of each X-ray sources was significant, and the corrected astrometry again was not significantly more accurate than the default pipeline values. Therefore, we expect that the astrometry will on average be accurate to  $0''.7$ , but that  $\approx 10\%$  of the pointings will have systematic errors of up to  $1''$ . Unfortunately, there is no way of knowing *a priori* which observations have the larger astrometric errors, so our astrometric accuracy is limited to  $\approx 1''$  in the shallower exposures.

In Table B1, we list the refined positions and positional uncertainties (90% confidence), which include statistical and systematic terms. For the statistical positional error, we use the count-rate-dependent estimates in Alexander et al. (2003). For the majority of sources with  $< 200$  net counts, we assume the uncertainty  $\Delta = 0''.6$  for offsets  $\theta \leq 5'$  and

$$\Delta = 0.6 + \left( \frac{\theta - 5'}{6.25'} \right) \text{ arcsec} \quad (1)$$

for  $\theta > 5'$ . For 19 bright sources with  $\geq 200$  net counts, we assume  $\Delta = 0''.3$  for offsets  $\theta \leq 5'$  and

$$\Delta = 0.3 + \left( \frac{\theta - 5'}{25'} \right) \text{ arcsec} \quad (2)$$

for  $\theta > 5'$ . We combine the statistical errors in quadrature with  $0''.7$  systematic uncertainties for the shallow observations (all those except ObsIDs 944 and 945, for which we assume no systematic uncertainty). In Table B1, we also list the observation in which a source was detected in, the offset from the aim point of that observation, and the total live time each source was observed with. We omitted two bright, previously-known LMXBs from the table (1E 1740.7–2942 and 2E 1743.1–2842), because they were badly saturated in our survey images, and their positions and properties are reported elsewhere (e.g., Martí et al. 2000; Porquet et al. 2003).

## 2.2. Photometry

We computed photometry for each source in the 0.5–8.0 keV band using the `acis.extract` routine from the Tools for X-ray Analysis (TARA).<sup>9</sup> We extracted event lists for each source for each observation, using an extraction region designed to enclose a large fraction of the PSF. We used a PSF at a fiducial energy of 1.5 keV for sources detected only in the soft band (flagged with a 'f' to indicate a possible foreground source in Tab. B1), while we used a larger extraction area corresponding to a PSF for 4.5 keV photons when sources were detected in the full or hard bands.

In most cases, we chose polygonal regions that matched the contours of 90% encircled energy from the PSF. However, if the 90% contours of the PSFs of two nearby

sources overlapped, we generally used a region that corresponded to a smaller fraction of the PSF. We have flagged these sources as confused ('c') in Table B1. The smallest extraction region that we used matched the 70% encircled energy contour. However, because the PSF grows significantly as a function of off-axis angle, in many cases a source that appeared isolated when it was located on-axis in one observation was indistinguishable from its neighbors in images from adjacent, overlapping pointings. We found that no reasonable fraction of the PSF would isolate counts from sources more than  $7'$  off-axis whose 90% encircled-energy radii overlapped those of their neighbors, so we did not extract photometry from observations in which confused sources were  $> 7'$  off-axis. Fortunately, these sources always lay near the aim point of another observation (or else they could not have been detected in the first place), so we were still able to obtain photometry for these sources.

For each source and each observation, a background event list was extracted from a circular region centered on the point source, excluding from the event list counts in circles circumscribing the  $\approx 92\%$  contour of the PSF around any point sources. We found that this value struck a good balance between excluding counts from point sources and leaving enough counts in the image to determine the background. The sizes of the background regions were chosen such that they contained approximately 100 events for each observation. Less than 1% of the counts in the background regions were from point sources. We also computed the effective area function (ARF) at the position of each source for each observation using the CIAO tool `mkarf`.

The source and background event lists were used to compute photometry for each source in five energy bands: 0.5–8.0 keV (the full band), 0.5–2.0 keV, 2.0–3.3 keV, 3.3–4.7 keV, and 4.7–8.0 keV. These bands are identical to those used by Muno et al. (2003) for the catalog of X-ray sources within 25 pc of Sgr A\*. The energy bands were chosen so that they sampled regions of the ARF with roughly constant areas, and so that the three high energy bands each contained about one-third of the net counts from most sources. The net counts in each band were computed by subtracting the estimated background from total counts. The 90% uncertainty in the net counts in each of the five bands were computed through a Bayesian analysis, with the simplifying assumption that the uncertainty on the background was negligible (Kraft, Burrows, & Nousek 1991). When the 90% confidence interval on the net counts was consistent with 0, we considered the upper bound on the 90% confidence interval to be the upper limit.

A histogram of the number of sources as a function of net counts in the full band is displayed in Figure 2. Most sources were detected with 10–20 counts in two overlapping 12 ks observations. Therefore, most sources were only observed with  $\approx 5$  counts in each of the smaller energy bands. The net counts from 303 sources are consistent with zero at the 90% level. About 70% of these sources are flagged in Table B1 because their photometry could be unreliable for various reasons: some are detected only in the soft band where the background is lower, some are variable so that the mean flux is not meaningful, and some are confused with nearby sources. The remaining  $\approx 90$  sources are probably spurious, as we

<sup>9</sup> [www.astro.psu.edu/xray/docs/TARA/](http://www.astro.psu.edu/xray/docs/TARA/)

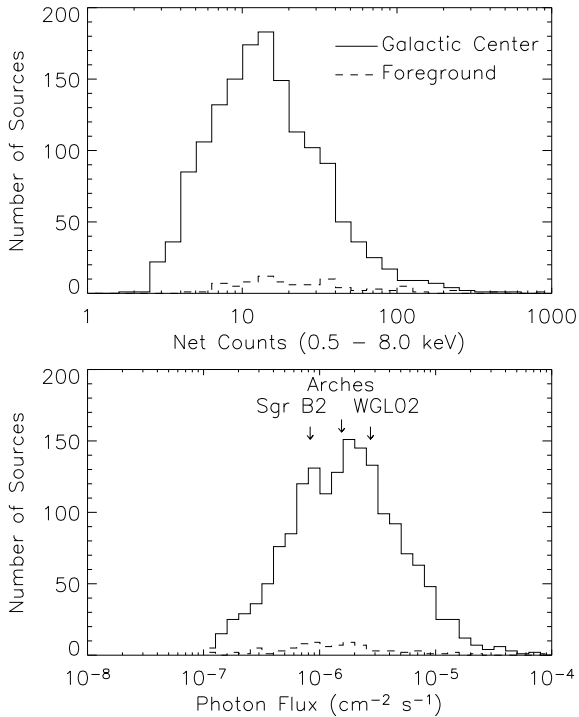


FIG. 2.— *Top panel:* The distribution in net counts from individual sources. No correction is applied to account for the exposure across the survey, which varies by a factor of 5. *Bottom panel:* The distribution of fluxes from individual sources, derived by dividing the net count rates by the effective area and exposure in four energy bands (0.5–2.0 keV, 2.0–3.3 keV, 3.3–4.7 keV, and 4.7–8.0 keV), and summing the result. There are two peaks, because the deeper observations were more sensitive to faint sources. In both panels, the solid line is used for sources located near or beyond the Galactic center ( $HR > -0.175$ ), and the dashed line for foreground sources ( $HR < -0.175$ ). The arrows denote the median sensitivity for the shallow survey (labeled WGL02) and for the deep Arches and Sgr B2 fields.

expected  $\approx 70$  spurious sources based on our detection threshold. We suspect we detected  $\approx 20$  more spurious than we expected because the background in our observations is  $\approx 10$  times larger than in the observations taken at high Galactic latitude with `wavdetect` was calibrated. We keep these potentially spurious sources in the catalog for completeness. The net counts and 90% uncertainties (or upper limits) are listed in Table B1. These values are used to compute the probability of detecting each source given its location and exposure, which is also listed in the table. The Monte Carlo simulations used to estimate this probability are described in Appendix A.

We computed approximate photon fluxes (in units of  $\text{ph cm}^{-2} \text{s}^{-1}$ ) for each source by dividing the net counts in each sub-band by the total live time (units of s) and the mean value of the ARF in that energy range (units of  $\text{cm}^2$ ; note that this value incorporates variations in exposure due to chip gaps and dead columns). The photon fluxes in the 0.5–8.0 keV energy band used throughout the paper are the sums of those in the sub-bands, using negative values when they occur (not the upper limits). They are listed in Table B1. We have found that the approximate photon fluxes that we computed differed from those derived from spectral fits by little more than the

Poisson uncertainty in the count rate, because the energy bands sampled the ARF for the ACIS-I detector well (Muno et al. 2003).

A histogram of the number of sources as a function of the 0.5–8.0 keV photon flux is presented in the *bottom panel* of Figure 2. Galactic center sources are indicated with the *solid line*, and foreground sources with the *dashed line*. Sources are detected with average photon fluxes as low as  $2 \times 10^{-8} \text{ ph cm}^{-2} \text{ s}^{-1}$ . The largest number of Galactic center sources are detected near  $2 \times 10^{-6} \text{ ph cm}^{-2} \text{ s}^{-1}$  (2.0–8.0 keV), and the largest number of foreground sources are found near  $1 \times 10^{-6} \text{ ph cm}^{-2} \text{ s}^{-1}$  (0.5–2.0 keV).

We used the counts in each energy band to compute two hardness ratios, which we used to characterize the absorption column toward each source and the steepness of the high-energy portion of each spectrum. The ratios are defined as the fractional difference between the count rates in two energy bands,  $(h - s)/(h + s)$ , where  $h$  and  $s$  are the numbers of counts in the higher and lower energy bands, respectively. The resulting ratio is bounded by  $-1$  and  $+1$ . The soft color is defined by the fractional difference between counts with energies between 2.0–3.3 keV and 0.5–2.0 keV, and the hard color using counts between 4.7–8.0 keV and 3.3–4.7 keV. The hardness ratios are listed in Table B1, with uncertainties calculated according to Equation 1.31 in Lyons (1991; page 26).

We use the soft color ( $HR0$ ) to identify foreground and highly-absorbed sources. By comparing the spectral fits and hard colors in (Muno et al. 2003, 2004b), we find that sources with  $HR0 > -0.175$  or that are not detected below 3.3 keV have absorption columns  $N_{\text{H}} > 4 \times 10^{22} \text{ cm}^{-2}$ , and are therefore likely to lie at or beyond the Galactic center. We refer to these as the “Galactic center sources,” of which there are 1350. Sources with  $HR0 < -0.5$  have  $N_{\text{H}} \lesssim 10^{21} \text{ cm}^{-2}$  and lie within 2 kpc of Earth. Sources with intermediate soft colors lie between 2–6 kpc from the Earth. The 549 sources with  $HR0 < -0.175$  that are likely to be closer than 6 kpc are considered foreground sources.

In Figure 3, we plot the hard color versus the flux from each source. Foreground sources are indicated with open circles, and sources at or beyond the Galactic center with filled circles. There are 785 Galactic center sources and 39 foreground sources with measured hard colors. We have calculated the hardness ratios and photon fluxes that we would expect to get from these energy bands for a variety of spectra and 0.5–8.0 keV luminosities using PIMMS and XSPEC. In Figure 3, we plot the colors and fluxes expected for power-law spectra with the dotted lines, and for an optically-thin thermal plasma with the solid lines. We have assumed a distance of 8 kpc and  $6 \times 10^{22} \text{ cm}^{-2}$  of absorption from interstellar gas and dust. The median hard color for the Galactic center sources is  $-0.05$ . This corresponds to a  $\Gamma=1.5$  power law or a  $kT=1.7$  keV plasma spectrum.

The Galactic center sources in this survey are significantly softer than those from the deeper (limiting luminosity of  $L_{\text{X}} = 2 \times 10^{31} \text{ erg s}^{-1}$ ) catalog from the central 20 pc of the Galaxy. The latter catalog had a median hard color of  $-0.22$  (Muno et al. 2003), corresponding to a  $\Gamma=0$  power law spectrum. This suggests that the more luminous X-rays sources are systematically softer.

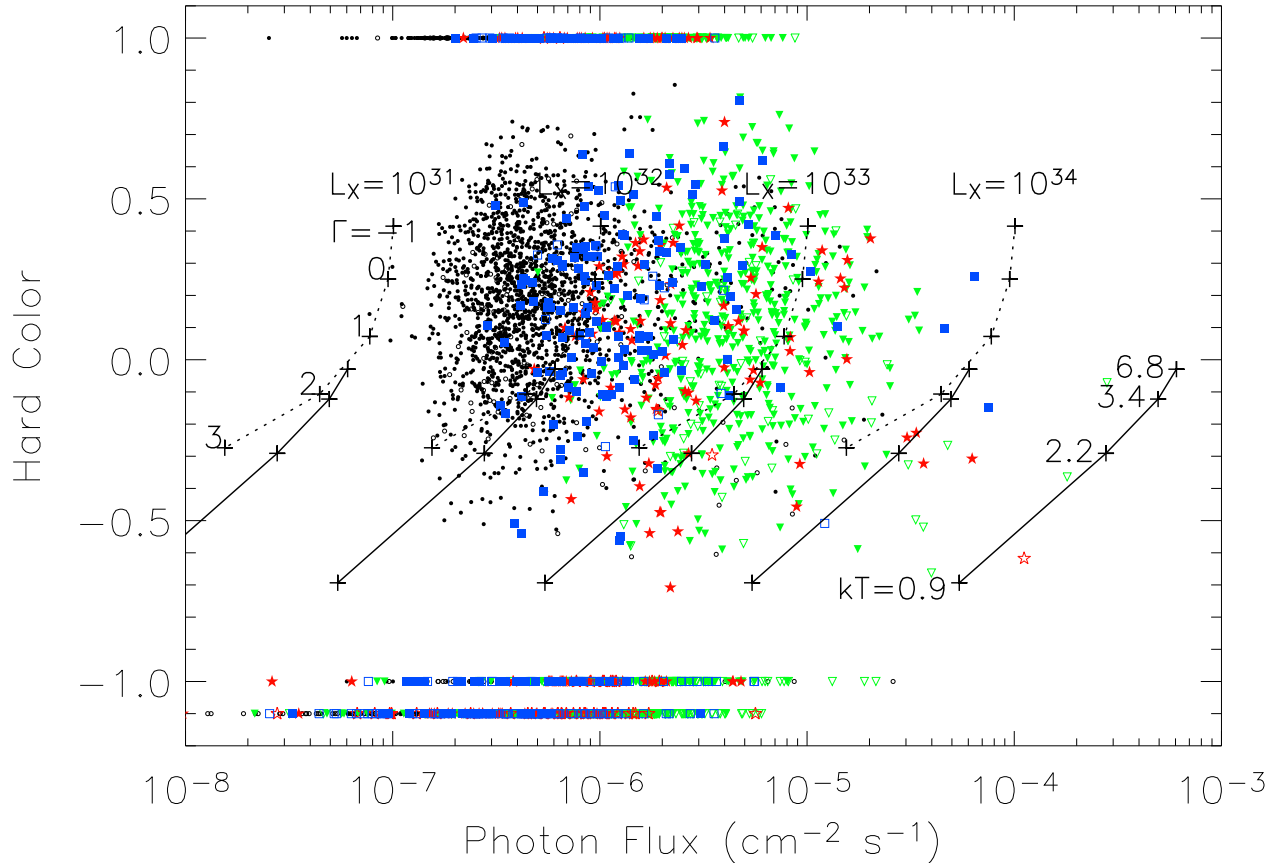


FIG. 3.— The hard color plotted against the photon flux from each source. The symbol shapes indicate which observations the sources were identified in: blue squares for the Sgr B2 field, red stars for the Arches region, and green triangles for the extended shallow survey. For comparison, we also include the data from the central 25 pc (Muno et al. 2003) using black circles. Open symbols indicate foreground sources, and filled circles those at or beyond the Galactic center (see text). Sources detected in only in the 3.3–4.7 keV band are assigned hard colors of  $-1$ ; those only detected in the 4.7–8.0 keV band are assigned  $HR2=+1$ , and those detected in neither band are assigned  $HR2=-1.1$ . The uncertainties on the hard colors are significant. Sources with a probability of  $<50\%$  of being detected have unreliable hard colors; those with a 50–90% chance of detection have  $\sigma_{HR2} \approx 0.6$ ; those with a 90–99% chance of detection have  $\sigma_{HR2} \approx 0.4$ ; and those with a  $>99\%$  chance of detection have  $\sigma_{HR2} \lesssim 0.3$ . Finally, we have plotted the colors expected for sources of varying luminosities at a distance of 8 kpc, and absorbed by  $6 \times 10^{22} \text{ cm}^{-2}$  of interstellar gas and dust. The dotted lines are for power-law spectra, and the solid lines for thermal plasma spectra. The sources with  $HR2 > 0.5$  either have large uncertainties, large absorption columns, or both. For a fiducial conversion factor between photon flux and 0.5–8.0 keV luminosity, we assume a  $\Gamma=1.5$  power law or a  $kT=7$  keV plasma, and find that  $10^{34} \text{ erg s}^{-1}$  equals  $6 \times 10^{-5} \text{ ph cm}^{-2} \text{ s}^{-1}$ .

For a fiducial  $\Gamma = 1.5$  spectrum absorbed by  $N_{\text{H}}=6 \times 10^{22} \text{ cm}^{-2}$ , the photon fluxes can be converted to energy fluxes according to  $1 \text{ ph cm}^{-2} \text{ s}^{-1} = 8 \times 10^{-9} \text{ erg cm}^{-2} \text{ s}^{-1}$  (0.5–8.0 keV). The de-absorbed 0.5–8.0 keV flux is approximately 3 times larger, so that for a distance  $D=8$  kpc,  $10^{34} \text{ erg s}^{-1}$  equals  $6 \times 10^{-5} \text{ ph cm}^{-2} \text{ s}^{-1}$ . For sources detected below 2.0 keV, we find that  $1 \text{ ph cm}^{-2} \text{ s}^{-1} = 2 \times 10^{-9} \text{ erg cm}^{-2} \text{ s}^{-1}$  between 0.5–2.0 keV. The absorption for these sources is relatively small ( $< 10^{22} \text{ cm}^{-2}$ ), and therefore so is the correction to derive an intrinsic flux.

### 3. RESULTS

#### 3.1. Spatial Distribution

We examined the spatial distribution of the X-ray sources in order to determine how it compares to that of the ordinary stellar population observed in the infrared. We were most interested in sources near the Galactic center, so we only considered those sources with

soft colors  $HR0 > -0.175$ . We also took care to select only sources that were bright enough to be detected over a large fraction of the survey. To do this, we derived maps of our sensitivity as described in Appendix A, and we examined only those sources that (1) were brighter than a well-defined flux limit, and (2) that were located at a position where the sensitivity was lower than that flux limit. Our flux limit was designed so that sources brighter than the limit have at least a 50% chance of being detected over a significant fraction of our survey (see Appendix A for a description of the Monte Carlo simulations that we used to calculate the detection probability). We found that a flux limit of  $3 \times 10^{-6} \text{ ph cm}^{-2} \text{ s}^{-1}$  (equivalent to  $5 \times 10^{32} \text{ erg s}^{-1}$  [0.5–8.0 keV] taking  $D=8$  kpc,  $N_{\text{H}} = 6 \times 10^{22} \text{ cm}^{-2}$ , and a  $\Gamma=1.5$  power law) provided the largest number of sources, 321 out of the 1899 sources in Table B1.

We then computed the surface density of sources as a function of offset from Sgr A\* and of the absolute val-

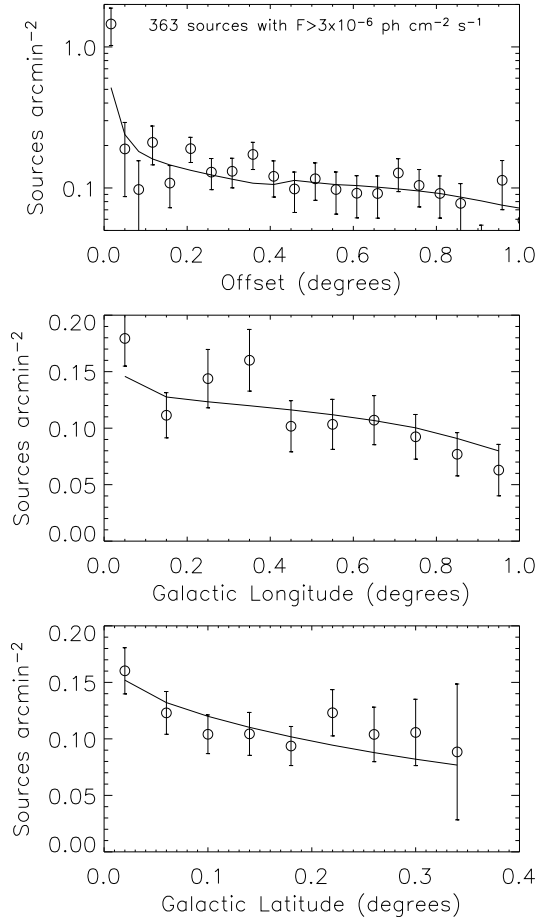


FIG. 4.— The distributions of point sources as a function of angular offset from Sgr A\* (*top panel*), and the absolute values of Galactic longitude (*middle panel*) and latitude (*bottom panel*). We only considered sources that were brighter than  $F_X = 3 \times 10^{-6}$  ph  $\text{cm}^{-2} \text{s}^{-1}$ , that had a 50% chance of being detected, and that lay in regions where the 50% detection threshold was lower than the above flux limit. The contribution of each source to the distribution was weighted by the inverse of the probability of detecting it. The surface density of stellar mass is plotted with the solid line, which has been normalized through a chi-squared minimization to match the surface density of X-ray sources. In all cases, the normalization implied that there were  $4 \times 10^{-7}$  X-ray sources with  $F_X \geq 3 \times 10^{-6}$  ph  $\text{cm}^{-2} \text{s}^{-1}$  for every  $1 M_\odot$  of stars.

ues of the Galactic latitudes and longitudes, and plotted them in Figure 4. To account for the variations in our sensitivity over the survey region, the contribution of each source to the distribution was weighted by the inverse of the probability of detecting it (calculated as described in Appendix A). We used the catalog of Muno et al. (2003) to fill in the inner  $8'$  around Sgr A\*. We used the identical flux cuts in the Sgr A\* field as for the rest of the survey, which allowed us to include another 42 sources.

To compare the distribution of X-ray sources with that of the ordinary stellar population, we used models for the Galactic bulge and the central 150 pc that were derived from infrared maps by Launhardt et al. (2002), and the exponential model of the Galactic disk in Kent, Dame, & Fazio (1991). These mass models are accurate to about

50%. We modeled the central 150 pc with two components. We assumed that the central 15 pc is dominated by a spherical cluster with a mass density profile

$$\rho = \frac{\rho_c}{1 + (r/r_c)^n}. \quad (3)$$

For  $r < 6$  pc, we use  $\rho_c = 3.3 \times 10^6 M_\odot \text{pc}^{-3}$ ,  $r_c = 0.22$  pc, and  $n = 2$ . For  $6 < r < 200$  pc,  $n = 3$ ,  $r_c$  remains the same, and  $\rho_c$  is adjusted so that the function is continuous at  $r = 6$  pc. The total mass of the central cluster is  $6 \times 10^7 M_\odot$ .

The rest of the central 150 pc is dominated by a disk-like distribution with a mass density

$$\rho = \rho_d r^{-n} \exp(-|z|/z_d). \quad (4)$$

For  $r < 120$  pc, we take  $\rho_d = 300 M_\odot \text{pc}^{-3}$ ,  $n = 0.1$ , and  $z_d = 45$  pc. For  $120 < r < 220$  pc, we take  $n = 3.5$ , leave  $z_d$  the same, and adjust  $\rho_d$  so the function is continuous at  $r = 120$  pc. For  $220 < r < 2000$  pc, we take  $n = 10$ , and treat the other parameters the same as above. The total mass of this nuclear stellar disk is  $1.4 \times 10^9 M_\odot$ .

We model the Galactic bulge as a tri-axial ellipsoid of the form

$$\rho = \rho_{\text{bulge}} e^{-r_s} \quad (5)$$

$$r_s = \left[ (r_\perp)^{c_\parallel} + \left( \frac{|x|}{a_x} \right)^{c_\parallel} \right]^{1/c_\parallel} \quad (6)$$

$$r_\perp = \left[ \left( \frac{|x|}{a_x} \right)^{c_\perp} + \left( \frac{|y|}{a_y} \right)^{c_\perp} \right]^{1/c_\perp}. \quad (7)$$

The axis defining  $x, y, z$  is rotated  $15^\circ$  in east and  $1^\circ$  north from our line-of-sight. The parameters are  $a_x = 1100$  pc,  $a_y = 360$  pc,  $a_z = 220$  pc,  $c_\perp = 1.6$ , and  $c_\parallel = 3.2$ , and  $\rho_{\text{bulge}} = 8 M_\odot \text{pc}^{-3}$ . The total mass of the bulge is taken to be  $10^{10} M_\odot$ .

Finally, we model the Galactic disk as a simple exponential,

$$\rho = \rho_0 \exp(-r/r_d) \exp(-|z|/z_d), \quad (8)$$

where  $r_d = 2.7$  kpc,  $z_d = 200$  pc, and  $\rho_0 = 5 M_\odot \text{pc}^{-3}$ , so that the total mass of the disk is  $10^{11} M_\odot$ .

We integrated the model stellar density along our line of sight toward the Galactic center, using a lower limit of 6 kpc because we excluded foreground sources from the profiles in Figure 4, and an upper limit of 10 kpc because sources beyond this distance will be heavily absorbed and difficult to detect. We then compared these model surface densities to the observed surface density of X-ray sources through a linear  $\chi^2$  minimization. We did not attempt to correct the surface density of X-ray sources to account for fact that the absorption column varies as a function of longitude, latitude, and along our line of sight in the image, because the uncertainty introduced by our failure to do so is smaller than the  $\approx 50\%$  uncertainty in the mass model. The best-fit stellar surface densities are indicated by solid lines in Figure 4. The overall match is good, with  $\chi^2/\nu < 1$ . However, within  $2'$  of Sgr A\* (4.7 pc in projection) the number of X-ray sources is  $2\sigma$  larger than that expected from a simple scaling of the mass distribution inferred from the infrared ( $1.3 \pm 0.4$  sources  $\text{arcmin}^{-2}$  versus the predicted 0.5 sources  $\text{arcmin}^{-2}$ ). This may be further evidence that X-ray sources are more concentrated near Sgr A\* than ordinary stars are (see also Muno et al. 2005a).

TABLE 2  
PARAMETERS OF THE  $\log N - \log S$  DISTRIBUTION

| Field          | $S_{\text{lim}}$<br>$10^{-6} \text{ ph cm}^{-2} \text{ s}^{-1}$ | Num.<br>Sources | Area<br>(arcmin <sup>2</sup> ) | $\alpha$      | $N_0$<br>(arcmin <sup>-2</sup> ) | $P_{\text{KS}}$ |
|----------------|---|-----------------|--------------------------------|---------------|----------------------------------|-----------------|
| Sgr B2         | 0.7   | 48              | 101                            | $1.7 \pm 0.2$ | 0.04                             | 0.99            |
| Radio Arches   | 2   | 28              | 97                             | $1.1 \pm 0.2$ | 0.17                             | 0.69            |
| Shallow Survey | 6   | 142             | 2833                           | $1.5 \pm 0.1$ | 0.11                             | 0.37            |
| Sgr A*         | 0.8   | 232             | 152                            | $1.4 \pm 0.1$ | 0.24                             | 0.20            |

NOTE. — The normalization of the  $\log N - \log S$  distribution,  $N_0$  is listed for a fiducial flux of  $3 \times 10^{-6} \text{ ph cm}^{-2} \text{ s}^{-1}$ , to match the spatial distribution in Figure 4.  $P_{\text{KS}}$  represents the probability under a Kolgoromov-Smirnov test of seeing the observed difference between the observed and model distribution assuming that they are identical, so that very small values would indicate a poorer match.

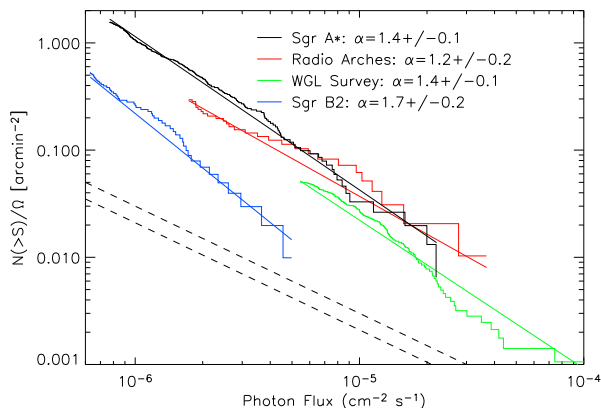


FIG. 5.— The number-flux distribution of sources in the Arches Region (red lines), the Sgr B2 region (blue lines), and the shallow survey (blue lines). The solid histograms have been corrected for the detection probability, and are only plotted for sources brighter than the flux limits used in modeling the distributions. The solid lines are the best-fit model distributions ( $N(> S) \propto S^{-\alpha}$ ), with the slopes indicated in the upper-right of the figure. The dashed lines represent the background AGN contributions taken from Brandt et al. (2001) and Manners et al. (2003).

The normalization of the fits imply that above a limit of  $5 \times 10^{32} \text{ erg s}^{-1}$  there are  $(4 \pm 2) \times 10^{-7}$  X-ray sources per solar mass of stars, where most of the uncertainty is in the mass models. We compare this to the expected density of X-ray sources in §4.

### 3.2. Number-Flux Distribution

Spatial variations in the underlying population of X-ray sources could be identified by examining the relative number of faint and bright X-ray sources. Therefore, we have computed the cumulative  $\log N - \log S$  distributions in four regions: the Arches field, the Sgr B2 field, and the general shallow survey (excluding the deep pointings), and the Sgr A\* field (see also Muno et al. 2003). However, in this case, we required that each source had at least a 90% chance of being detected, which was stricter than when we studied the spatial distribution. We modeled the differential number-flux distribution using the method described in Murdoch, Crawford, & Jauncey (1973), with slight modifications described in Appendix B to use Poisson statistics and knowledge of the average background rate. As for the spatial distribution, we

defined a flux limit ( $S_{\text{lim}}$ ) for each region above which we could securely detect sources over the largest possible area. For the  $\log N - \log S$  distribution, we added the criterion that the flux limit allow us to measure the fluxes of sources at the  $5\sigma$  level. Our choice of flux limits is described in more detail in Appendix B. The flux limits, area covered by each survey, and number of sources that were brighter than  $S_{\text{lim}}$  and located at points where sources with  $S=S_{\text{lim}}$  could be detected securely are listed in Table 2.

In Table 2, we also list the best-fit slopes  $\alpha$ , the normalizations  $N_0$  at  $S_0=3 \times 10^{-6} \text{ ph cm}^{-2} \text{ s}^{-1}$  (the fit had to be extrapolated for the shallow survey), and the probabilities  $P_{\text{KS}}$  that the model and observed distributions match according to the KS-test. The increase in the normalization of the distributions is consistent with the radial distribution of point sources in Figure 4. We find marginal,  $1.8\sigma$  evidence that the  $\log N - \log S$  distribution is flatter in the Radio Arches region than in the Sgr B2 field or the survey as a whole, which would imply that the former contains a larger proportion of high-luminosity sources. Unfortunately, our constraints on the  $\log N - \log S$  distribution are a bit poor, because the number of sources that meet the criterion of having  $>5\sigma$  flux measurements (roughly,  $> 25$  photons) is small (see Fig. 2). The best-fit distributions are plotted with solid lines in Figure 5.

In Figure 5, we also plot the expected distributions of background active galactic nuclei (AGN). To convert between the photon fluxes we use here and the 2–8 keV energy flux that is reported in papers on the *Chandra* and *XMM-Newton* deep fields, we assume that AGN are observed through an absorption column of  $12 \times 10^{22} \text{ cm}^{-2}$  and that their spectra are described by a  $\Gamma=1.5$  power law (the final results are not sensitive to a choice of  $\Gamma$  between 1.2 and 1.8). We find that a source with a 0.5–8.0 keV photon flux of  $S_0 = 3 \times 10^{-6} \text{ ph cm}^{-2} \text{ s}^{-1}$  in our survey would have a 2–8 keV flux of  $6 \times 10^{-14} \text{ erg cm}^{-2} \text{ s}^{-1}$  if it were located at high Galactic latitude. Based on the number-flux distribution in the deep fields, expected density of background AGN is given by  $N(> S) = N_0(S/S_0)^{-1}$ , where at  $S_0 = 3 \times 10^{-6} \text{ ph cm}^{-2} \text{ s}^{-1}$ ,  $N_0=0.007 \text{ source arcmin}^{-2}$  in Brandt et al. (2001), and  $N_0=0.01 \text{ source arcmin}^{-2}$  in Manners et al. (2003). This normalization is  $<10\%$  of that of the shallow survey in Table 2 (see also Fig. 4). We conclude that  $<130$  of the absorbed sources in our sample should be extra-galactic.



## 4. DISCUSSION

We have presented a catalog of X-ray sources with fluxes between a few  $10^{31}$  and  $10^{35}$  erg s $^{-1}$ . The majority of the region was covered with tiled pairs of 12 ks observations, in which the 50% completeness limit is  $1 \times 10^{33}$  erg s $^{-1}$ . Two deeper exposures were more sensitive. A 50 ks toward the Radio Arches was complete to  $4 \times 10^{32}$  erg s $^{-1}$ , and a 100 ks observations toward Sgr B2 was complete to  $1 \times 10^{32}$  erg s $^{-1}$ . The sensitivity of the Radio Arches observation was a factor of two poorer than would be naively expected based on the exposure time, because the Galactic center produces strong diffuse emission against which point sources are more difficult to detect.

Our survey encompasses a non-trivial fraction of the mass of stars in the Galaxy. Integrating the (Launhardt et al. 2002) models for the stellar distribution over our survey area, we find that it encloses a stellar mass of  $\sim 10^9 M_\odot$ , or 1% of the Galactic value. In Table 3, we list the various classes of object that could be detected as X-ray sources in our image if they were located near the Galactic center. We also include predictions for the total number of each class of sources encompassed by the survey region, based on the references in the table. The estimates are based on the assumption that the star formation rate is  $\sim 1\%$  of the Galactic value, or  $0.01 M_\odot \text{ yr}^{-1}$  (Figer et al. 2004). However, if the recent rate of star formation in the central 150 pc of the Galaxy is  $\sim 10\%$  of the total Galactic rate, as is suggested by indirect measurements of the Lyman-alpha flux in the region (Cox & Laureijs 1989; Figer et al. 1999), then WR/O stars, luminous pulsars, and high-mass X-ray binaries each could be an order-of-magnitude more numerous. Below we describe the considerations that went into developing that table, and some implications that the observed population of sources have for understanding the evolution of the accreting binaries that make up the majority of our sample.

## 4.1. Comparison to the Local Galactic X-ray Population

We start by comparing the amount of X-ray flux per unit stellar mass from the point sources with  $L_X > 5 \times 10^{32}$  erg s $^{-1}$  in our survey to that in the local Galaxy as identified by Sazonov et al. (2005). For a cumulative number-flux distribution of the form  $N(> L_X) = N_0(L_X/L_{X,0})^{-\alpha}$ , the specific luminosity produced by sources with  $L_{X,\min} < L_X < L_{X,\max}$  is

$$\mathcal{L}_{X,\text{tot}} = \frac{\alpha N_0 L_{X,0}}{\alpha - 1} \left[ \left( \frac{L_{X,\min}}{L_{X,0}} \right)^{-\alpha+1} - \left( \frac{L_{X,\max}}{L_{X,0}} \right)^{-\alpha+1} \right], \quad (9)$$

where  $N_0$  is the normalization at a luminosity of  $L_{X,0}$  in units of sources per solar mass. For the Galactic center, we have found that  $\alpha = 1.5$  and that  $N_0 = (4 \pm 2) \times 10^{-7}$  sources  $M_\odot^{-1}$  at  $L_{X,0} = 5 \times 10^{32}$  erg s $^{-1}$  (Tab. 2, Fig. 4). So, the specific luminosity of X-ray point sources with luminosities between  $L_{X,\min} = 5 \times 10^{32}$  erg s $^{-1}$  and  $L_{X,\max} = 10^{34}$  erg s $^{-1}$  in our survey is  $\mathcal{L}_{X,\text{tot}} = (5 \pm 2) \times 10^{26}$  erg s $^{-1} M_\odot^{-1}$ . In the local Galaxy, Sazonov et al. (2005) find that  $\alpha \approx 1.2$  and  $N_0 = (6 \pm 2) \times 10^{-4}$  sources  $M_\odot^{-1}$  at  $L_{X,0} = 2 \times 10^{30}$  erg s $^{-1}$  (where for  $K$  in their Eq. 5,  $N_0 = K/\alpha$ , and we have estimated the uncertainty based on that of total specific luminosity for sources with  $L_X < 10^{34}$  erg s $^{-1}$ ). So, the specific luminosity of sources

TABLE 3  
X-RAY SOURCES IN THE GALACTIC CENTER

| Object     | $\log(L_X)$<br>$\log(\text{erg s}^{-1})$ | Number<br>in GC | Number<br>Detectable | References |
|------------|--|-----------------|----------------------|------------|
| CVs        | 29.5–33.5                                | $10^5$          | $10^3$               | [1,2]      |
| WR/O Stars | 31–34                                    | $10^3$          | 10                   | [3,4,5]    |
| Pulsars    | 29.3–35                                  | $10^6$          | 10                   | [6,7]      |
| LMXBs      | 30–39                                    | $10^3$          | 10                   | [8,9,10]   |
| HMXBs      | 31–38                                    | $10^3$          | 50                   | [11]       |

REFERENCES. — [1] Verbunt et al. (1997); [2] Sazonov et al. (2005); [3] (Figer et al. 2004); [4] Pollock (1987); [5] Berghöfer et al. (1997); [6] Becker & Aschenbach (2002); [7] Cordes & Lazio (1997); [8] Wijnands et al. (2002); [9] Liu & Li (2005); [10] Kong et al. (2002a); [11] Pfahl et al. (2002).

NOTE. — We list order-of-magnitude estimates of the total population of various X-ray sources in our field, along with the number that should be detected in our survey.

with luminosities between  $L_{X,\min} = 5 \times 10^{32}$  erg s $^{-1}$  and  $L_{X,\max} = 10^{34}$  erg s $^{-1}$  is locally  $\mathcal{L}_{X,\text{tot}} = (1.0 \pm 0.3) \times 10^{27}$  erg s $^{-1} M_\odot^{-1}$ . Therefore, the specific luminosities of X-ray sources with  $5 \times 10^{32} < L_X < 10^{34}$  erg s $^{-1}$  in the local Galaxy and in the Galactic center are consistent within their uncertainties.

To understand the population of X-ray sources at the Galactic center, it is notable that in the local Galactic neighborhood all the X-ray sources with  $10^{32} < L_X < 10^{34}$  erg s $^{-1}$  (2–10 keV) are cataclysmic variables (CVs) with magnetic white dwarfs and orbital periods of several hours (intermediate polars; Sazonov et al. 2005). Therefore, it is conceivable that most of the X-ray sources with  $L_X < 10^{34}$  erg s $^{-1}$  in our survey are magnetic CVs (see also Munro et al. 2004b; Laycock et al. 2005). We would expect CVs to have the same spatial distribution as the old ( $\gtrsim$  Gyr) population of stars, which dominate the infrared light from the Galaxy, and indeed the distribution of X-ray sources is identical to the inferred distribution of stars (Fig. 4). As described in Munro et al. (2004b), intermediate polars have particularly hard, intrinsically-absorbed spectra that are consistent with those of the sources with  $L_X \lesssim 10^{33}$  erg s $^{-1}$  in Figure 3.

Few CVs have  $L_X > 10^{33}$ , and only one CV has been observed at  $L_X \gtrsim 5 \times 10^{33}$  erg s $^{-1}$  (GK Per in outburst; e.g., King, Ricketts, & Warwick 1979), so we expect brighter sources to be more luminous objects such as LMXBs, HMXBs, WR/O stars in colliding-wind binaries, or pulsars (Table 3). The excess of bright X-ray sources observed in the Radio Arches field (Fig. 5), in which the Arches and Quintuplet clusters are striking evidence recent active star formation (Figer et al. 1999), can be explained if some of the bright sources are HMXBs, WR/O stars, or young pulsars. Such sources have short lifetimes, and so should be concentrated near regions of active star formation. Such sources also have softer spectra than intermediate polars in the 2–8 keV band, and so could explain why the sources brighter than  $\sim 10^{33}$  erg s $^{-1}$  in Figure 3 are systematically softer than the faint ones.

## 4.2. Comparison to Theoretical Models

Several binary population synthesis calculations have been carried out in order to interpret the population

of X-ray sources in the Galactic center described by Wang et al. (2002) and Muno et al. (2003). These models outline how the numbers of each class of X-ray sources constrain various combinations of parameters in the binary evolution models and assumptions about the physics of systems accreting at low rates.

For instance, Pfahl et al. (2002) suggested that several hundred of the X-ray sources in the Wang et al. (2002) survey could be neutron stars accreting from the winds of  $>3M_{\odot}$  binary companions (see also Belczynski & Taam 2004). The total numbers of wind-accreting neutron stars, and the fractions of systems with companions more and less massive than  $8M_{\odot}$ , varies by a factor of a few depending upon the the magnitudes of the kicks imparted to the neutron stars at birth. These theoretical predictions have motivated searches for infrared counterparts to the X-ray sources in the Galactic center surveys (Laycock et al. 2005; Bandyopadhyay et al. 2005). However, Liu & Li (2005) suggested that accretion could be inhibited by the magnetospheres of the neutron stars (see also Davies & Pringle 1981) at the low mass-transfer rates considered by Pfahl et al. (2002), so that wind-accreting neutron stars may not be luminous enough to be detected in our *Chandra* survey.

There also is theoretical disagreement as to whether CVs contribute significantly to the population of X-ray sources in our survey. Liu & Li (2005), who base their calculations on the binary evolution code of Hurley, Tout, & Pols (2002), suggest that CVs are not luminous enough to be detected in large numbers from the Galactic center. However, this disagrees with similar calculations by Ruiter et al. (2005), who use the StarTrack code (Belczynski et al. 2005), and predict that significant numbers of luminous CVs should be detectable from the Galactic center. The main difference between the two codes is in their prescriptions for calculating the rate of mass transfer, which leads Liu & Li (2005) to predict mass transfer rates  $\sim 100$  times lower than those used by Ruiter et al. (2005) for identical systems with orbital periods of several hours (A. Ruiter, private communication). Systems with orbits of several hours have the highest accretion rates (Patterson 1984, see also Howell, Nelson, & Rappaport 2001) and therefore are the most luminous in X-rays, which makes them the most important contributors among CVs to our survey. Our comparison with the local Galactic population of X-ray sources suggests that CVs are indeed both numerous and luminous enough to explain the population of X-ray sources in our image (see also, e.g., Verbunt et al. 1997; Ezuka & Ishida 1999; Suleimanov, Revnivtsev, & Ritter 2005), so our results could be taken as further, indirect evidence in support of the prescription used by Belczynski et al. (2005) and Ruiter et al. (2005).

Finally, Belczynski & Taam (2004) and Liu & Li (2005) predict that there are a few thousands LMXBs consisting of a neutron star accreting from a white dwarf in our survey region. In these models, most of the neutron stars in these systems form through the accretion-induced collapse of an ONe white dwarf. Under the assumptions of Liu & Li (2005), a few percent of the LMXBs are persistently bright enough to be detected in our survey. Moreover, most of these LMXBs should be transient, so if one assumes a standard duty cy-

cle of  $\sim 1\%$ , there should be  $>50$  LMXBs in outburst with  $L_X > 10^{36}$  erg  $s^{-1}$  in the field at any given time (and thousands in the Galaxy). In contrast, there are only two persistent LMXBs this luminous in the field, 1E 1743.1–2843 and 1E 1740.7–2942 (Wang et al. 2002), and several decades of occasional X-ray observations have only revealed about a dozen transients with  $L_X \gtrsim 10^{36}$  erg  $s^{-1}$  (and only  $\sim 150$  in the rest of the Galaxy; see, e.g., Liu, van Paradijs, & van den Heuvel 2001; Wijnands et al. 2005). The production of a large number of these transient LMXBs appears to be a common feature of models in which neutron stars can form through accretion-induced collapse (e.g., §5.6 of Iben, Tutukov, & Yungelson 1995). Under the models of Belczynski & Taam (2004) and Liu & Li (2005), possible ways to accommodate the small number of bright transients in our field are to assume that the efficiency with which the envelope of a star can be ejected during the common envelope phase is low so that many of the binaries merge rather than forming LMXBs, or to assume that the accretion-induced collapse of an ONe white dwarf does not form a neutron star.

## 5. THE FUTURE

Further progress in understanding the natures of the X-ray sources near the Galactic center, and the consequential constraints on the parameters input into binary evolution and population synthesis models, will be acquired through multi-wavelength observations of the region. X-ray observations will add to the population of transient LMXBs in the field (Wang et al. 2002; Sakano et al. 2005; Muno et al. 2005a; Wijnands et al. 2005, e.g.). Comparing infrared and X-ray surveys will reveal individual examples of WR/O binaries and HMXBs (Bandyopadhyay et al. 2005; Muno et al. 2005b, e.g.). The first pulsars near the Galactic center may be found by comparing radio and X-ray surveys (see also Cordes & Lazio 1997).

Finally, we note that this catalog will be improved upon greatly in the next year, because a series of deep, 40 ks exposures of roughly half of the survey area have been approved for the 2006 *Chandra* observing cycle. We expect to increase the number of X-ray sources detected by a factor of  $\approx 5$ , and improve the uncertainties on the positions of the sources in the shallow survey from  $\approx 1''$  to  $< 0.5''$ . In the meantime, the current catalog provides the best available sample for studying the spatial and number-flux distributions of X-ray sources near the Galactic center, and for identifying their counterparts at other wavelengths.

We thank M. Morris for comments on the manuscript, K. Belczynski for discussions about population synthesis models, and especially A. J. Ruiter and X. Liu for performing calculations to help clarify the differences between various population synthesis codes. MPM and FEB acknowledge support from NASA/SAO under grant AR5-6018A, and WQD acknowledges support from NASA/SAO under grant GO4-5010X. MPM also was supported under a Hubble Fellowship, and FEB under a Chandra Fellowship.

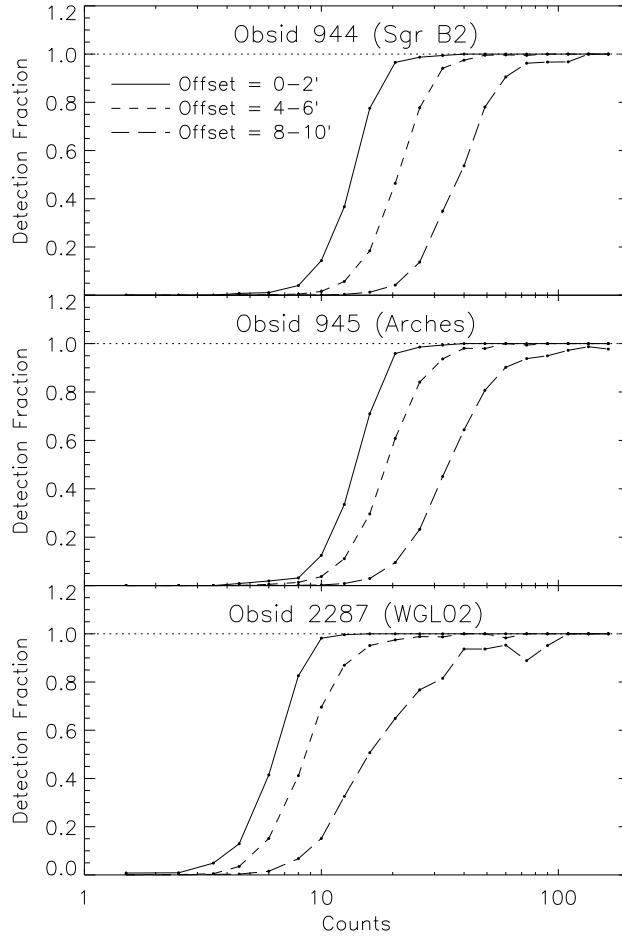


FIG. A1.— The probability of detecting a source as a function of count rate (y-axis) and offset (line styles). The detection probability depends upon the survey region because of variations in the diffuse X-ray background; the longer observations are background-limited. The probability at a given count rate decreases as the offset increases, because the size of the PSF increases. We note that the curve for the 8–10' offset in the shallow (WGL02) survey was not used much, because sources in that survey almost always were found closer to the aimpoint of at least one of the tiled pointings.

## APPENDIX

### COMPLETENESS OF THE SURVEY

In order to study the spatial and luminosity distributions of the X-ray sources, we need to calculate the limiting flux at which we can confidently detect sources as a function of position in the survey. We performed synthetic star tests following the basic method of Bauer et al. (2004), with modifications to account for differences in our treatment of the photometry and the more complex layout of our survey.

In order to produce  $\sim 10^5$  synthetic stars, we simulated 1000 exposures of ObsID 2287 (12 ks exposure), and 100 each for ObsIDs 945 (50 ks exposure), and 944 (100 ks exposure). For each observation, we removed events from within a circle circumscribing 92% of the energy of the PSF around each detected source. We then created images from the resulting event lists, and filled the “holes” in the image with a number of counts drawn from a Poisson distribution with a mean equal to that of a surrounding annulus. We drew fluxes for synthetic stars from a power-law distribution  $N(> S) \propto S^{-\alpha}$  with a slope  $\alpha = 1.5$ , normalizations and flux limits chosen to match the numbers and intensities of sources in each region (e.g., Tab. 2). We converted these fluxes to count rates using an exposure map generated for photons with  $E = 3$  keV, and then drew net numbers of counts from Poisson distributions with those mean count rates. Each point source was assigned to a random position in the image. Next, we obtained a model image of the PSF created by `mkpsf` when computing the photometry for the the nearest detected source in the image, and used the PSF as the probability distribution to simulate the 2-dimensional image of the counts. This was placed into the composite image. Finally, we search the synthetic image for point sources using `wavdetect`, and tabulated which sources we placed into the image were detected by our search algorithm.

We display the fraction of sources that are detected in 12, 50 and 100 ks as a function of input flux and offset from

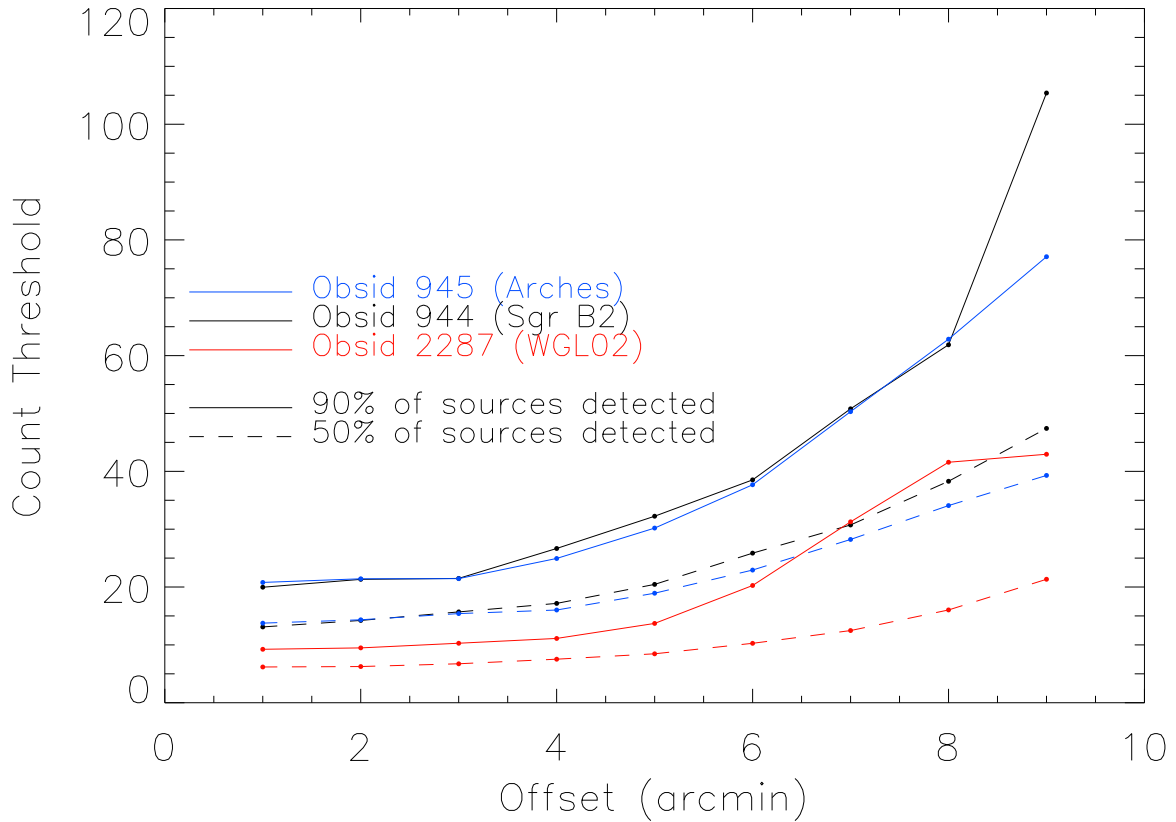


FIG. A2.— The number of counts required to detect a source in 50% (dashed line) and 90% (solid line) of trials, as a function of offset from the center of the cluster. In order of decreasing number of counts required, the red line is for the Arches region, the blue line for Sgr B2, and the green line for the shallow survey.

the aim point in Figure A1. The probability of detecting a source obviously increases with larger flux, because there is more signal-to-noise. For a given flux, the probability of detecting a source is also larger at small offsets from the aim point, because farther from the aim point counts are spread over a larger area by the PSF. This latter trend can also be seen in Figure A2, where we have plotted the number of counts above which a source will be detected 50% and 90% of the time as a function of offset from the aim point. As expected, longer observations enable us to reliably detect sources with lower fluxes. However, the total background counts from diffuse X-ray emission toward the Galactic center also increases for longer exposures, so more counts are required to reliably detect a source. As a result, a factor of 5 increase in exposure from 10 to 50 ks yields only a factor of 3 increase in sensitivity, which is by no means linear, but it is still a faster improvement than the  $t^{-1/2}$  trend that would be expected if we were background limited.

We used the above simulations to make a map of the sensitivity of our survey. For each observation, we generated a sensitivity map by (1) computing the offset of each pixel from the aim point, (2) computing the count threshold from Figure A2, and (3) dividing the count threshold by the exposure map (in units of  $\text{cm}^2 \text{s}$ ) to obtain a flux. Then, to create a composite map for the full survey, for each pixel we recorded the lowest value of the flux threshold from all of the maps with exposure at that pixel. We note that using this method, localized enhancements in the diffuse emission that decrease our sensitivity have been averaged over offset from the aim point. Properly accounting for all of the variations in the diffuse emission would require that we carry out our Monte Carlo simulations for each exposure, which would be time consuming and would not change our results significantly. The resulting map is displayed in Figure A3. We also have tabulated the area over which our survey is sensitive as a function of limiting flux, and displayed that in Figure A4.

We have also used the simulations to compute the probability of detecting each source. For each source, we determined the offset from the aim point of the most sensitive exposure, and determined the count threshold at that offset from Figure A2. We then divided that count threshold by the exposure map from the most sensitive observation at the location of the source to obtain a flux threshold. Again, this technique ignores local background variations that introduce systematic errors in our computed thresholds for individual sources, but these errors should average out when considering large numbers of sources. The median probability of detecting a Galactic center source was 57%.

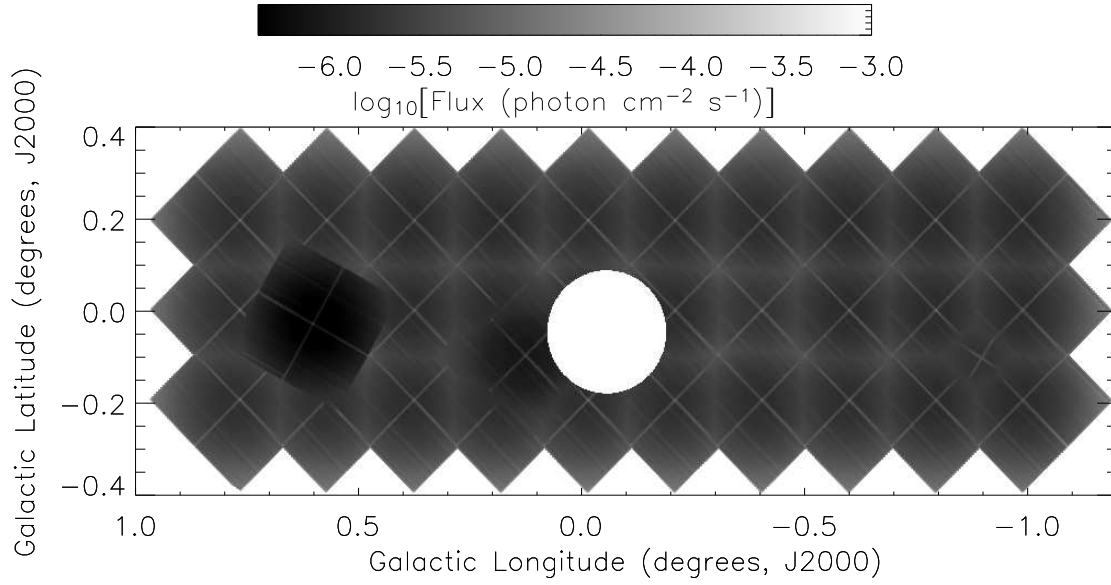


FIG. A3.— Map of the 50% detection threshold over our survey. The large white circle at the center represents the region covered by the deep survey in Muno et al. (2003). We do not include sources in that region in our catalog.

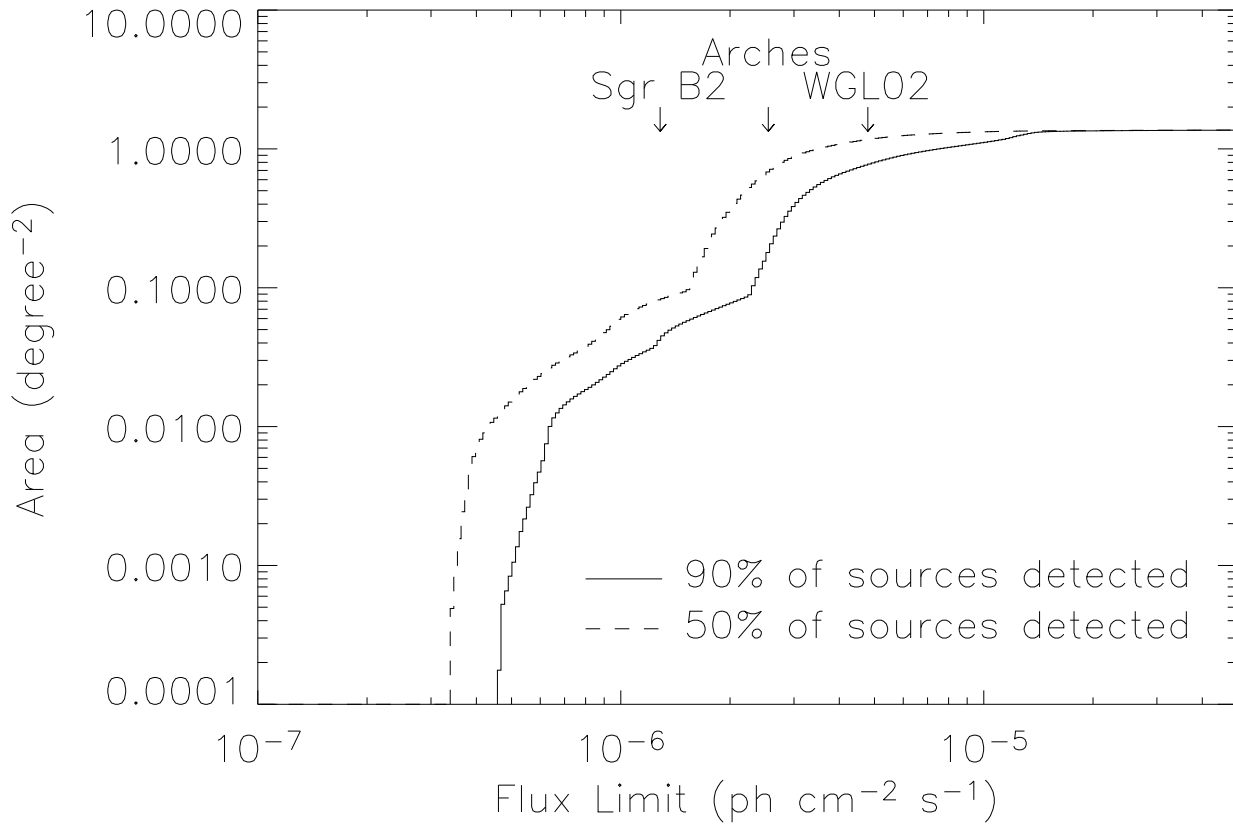


FIG. A4.— The area over which we were sensitive to sources of given fluxes. The mean sensitivity of the Sgr B2, Arches Region, and shallow surveys are indicated with arrows.

This is because the photons from faint sources are often lost to the wings of the PSF, and because the number-flux distribution is quite steep (see §3.2), so many faint sources are only detectable when Poisson fluctuations result in larger observed counts (this produces the Eddington bias when computing number-flux distribution).

The sensitivity maps and detection probabilities were used in computing the spatial distribution in §3.1 and flux distributions in §3.2. We also repeated the above process for the combined image created from 625 ks of exposure on the  $17' \times 17'$  field around Sgr A\*, so that we could compare the results from the catalog in Muno et al. (2003) to the current one. We find that a source can be detected confidently with the fewest counts in the shallow survey (Fig. A2), because the longer observations were background limited. Of course, the observations were still more sensitive when the detection threshold was considered as a function of flux (Fig. A4).

### MODELING THE NUMBER-FLUX DISTRIBUTION

We modeled the un-binned number-flux distributions using the technique described in Murdoch et al. (1973). We assumed that the cumulative number-flux distribution could be described as a power law  $N(> S) \propto S^{-\alpha}$ , where  $S$  is the net number of counts for a source, and that the number of observed counts could be described by a Poisson distribution with mean rate  $S + B$ , where  $B$  is the average number of background counts in the source extraction region (e.g.,  $B=4.3$  for the shallow survey). The likelihood of observing sources with a distribution of total counts  $C_i$  (which are all integers) is then:

$$\sum_i \ln P(C_i) = \sum_i P_{\text{det},i} K^{-1} \int_0^\infty \frac{e^{-(S+B)} (S+B)^{C_i}}{C_i!} N_0 S^{-(\alpha+1)} dS, \quad (\text{B1})$$

where  $K$  is normalization over the range of count rates under consideration ( $C_1, C_u$ ),

$$K = \int_0^\infty \sum_{C_1}^{C_u} P_{\text{det},i} \frac{e^{-(S+B)} (S+B)^{C_i}}{C_i!} N_0 S^{-(\alpha+1)} dS. \quad (\text{B2})$$

The normalization of the power law  $N_0$  drops out of Equation B1, and so it was derived by setting the normalization  $K$  for the best-fit  $\alpha$  equal to the observed number of sources. Finally, we compared the observed cumulative flux distribution to the model distribution  $P_i$  using a KS-test, to establish whether our power-law model is consistent with the data.

Caution needs to be used in exercising these equations, as is described in detail in Murdoch et al. (1973). First, the integrals over  $S$  will diverge as  $S$  approaches 0 unless a the count rate from a source is inconsistent with the background rate  $B$  at the  $\approx 5\sigma$  level (Murdoch et al. 1973; Wang 2004). Therefore, we restricted our analysis to sources brighter than the  $5\sigma$  detection threshold for the average background level in each region. The mean background and count thresholds are listed in Table 2. In doing so, we were able to ignore the negligible contributions to the above integrals from beyond  $S \approx (C_i) \pm 12(C_i)^{1/2}$ . Second, our source-detection algorithm was designed primarily to reject false positives, and we find that false negatives occur for  $\approx 20\%$  of sources with count rates at the  $5\sigma$  level above background. We use the factor  $P_{\text{det},i}$  in the above equations to account for the probability of detecting a source with a count rate  $C_i$ , which we determined from our Monte Carlo simulations. Third, in order to avoid being biased by bright sources detected in regions with poor sensitivity, we only considered regions of the image in which there was a  $>90\%$  chance of identifying a source with a flux equal to the  $5\sigma$  detection threshold. We list in Table 2 the number of sources that met these criteria and the area over which we were sensitive. Finally, we note that we used average values for the background and the detection probability, even though both varied significantly over the regions covered by each set of observations. The total counts  $C_i$  used above were the sum of the net counts derived from our photometry and the average background, which was then rounded to the nearest integer. This was necessary to ensure that the integrand in Equations B1 and B2 were monotonic functions of  $C_i$  (see also Wang 2004).

Our approach to modeling the  $\log N - \log S$  distribution takes into account the possible Eddington bias, although it ignores the vast majority of faint sources. Different approaches are possible, and should yield similar results. For instance, Bauer et al. (2004) used Monte Carlo simulations to estimate the corrections to the flux required to offset both the Eddington bias and biases introduced by their method for deriving the photometry for each source, assumed that the photometric uncertainties were negligible, and analytically computed  $\alpha$  from a maximum-likelihood distribution using corrected fluxes and the equations in Murdoch et al. (1973). We have not implemented this technique, because our procedure for computing the photometry for each source was computationally prohibitive to incorporate it into our Monte Carlo simulations. We also note that their resulting slope could be somewhat biased, because they have assumed a  $\log N - \log S$  distribution in computing the flux correction, thereby pre-determining the effect of the Eddington bias.

Wang (2004) has presented a method that is almost equivalent to ours, in which he applied a redistribution matrix to convert a model distribution into an observed distribution, and then found best-fit parameters for the model using the chi-squared and Cash minimization techniques implemented in XSPEC (Arnaud et al. 1996). If the model and un-binned fluxes are compared using the Cash statistic (Cash 1979), the techniques are equivalent, although the use of a response matrix converts the integral in Equation B1 into a sum. Using binned data and a chi-squared test obviously requires enough sources per bin that their numbers are approximately distributed as a Gaussian. That technique has the advantage of using tools that X-ray astronomers are familiar with, although it is conceptually more complicated

than our method.

## REFERENCES

- Alexander, D. M. et al. 2003, *AJ*, 126, 539  
 Arnaud, K.A., 1996, *Astronomical Data Analysis Software and Systems V*, eds. Jacoby G. and Barnes J., p17, ASP Conf. Series volume 101  
 Baganoff, F. K. et al. 2003, *ApJ*, 591, 891  
 Bandyopadhyay, R. M. et al. 2005, *MNRAS* in press, astro-ph/0509346  
 Bauer, F. E., Alexander, D. M., Brandt, W. N., Schneider, D. P., Treister, E., Hornschmeier, A. E., & Garmire, G. P. 2004, *AJ*, 128, 2048  
 Becker, W. & Aschenbach, B. 2002, *MPE Report* 278, p. 63  
 Berghöfer, T. W., Schmitt, J. H. M. M., Danner, R., & Cassinelli, J. P. 1997, *A&A*, 322, 167  
 Belczynski, K. & Taam, R. E. 2004, *ApJ*, 616, 1159  
 Belczynski, K., Kalogera, V., Rasio, F. A., Taam, R. E., Zezas, A., Bulik, T., Maccarone, T. J. & Ivanova, N. 2005, astro-ph/0511811  
 Brandt, W. N., 2001, *AJ*, 122, 2810  
 Cash, W., *ApJ*, 228, 939  
 Cordes, J. M. & Lazio, T. J. W. 1997, *ApJ*, 475, 557  
 Cox, P., & Laureijs, R. 1989, in *IAU Symp.* 136, *The Center of the Galaxy*, ed. M. Morris (Dordrecht: Kluwer), 121  
 Davies, R. E. & Pringle, J. E. 1981, *MNRAS*, 196, 209  
 de Pree, C. G., Goss, W. M., & Gaume, R. A. 1997, *ApJ*, 489, 143  
 Ezuka, H. & Ishida, M. 1999, *ApJS*, 120, 277  
 Figer, D. F., Kim, S. S., Morris, M., Serabyn, E., Rich, R. M., & McLean, I. S. 1999, *ApJ*, 525, 750  
 Figer, D. F., Rich, M. R., Kim, S. S., Morris, M., & Serabyn, E. 2004, *ApJ*, 601, 319  
 Freeman, P. E., Kashyap, V., Rosner, R., & Lamb, D. Q. 2002, *ApJS*, 138, 185  
 Howell, S. B., Nelson, L. A., & Rappaport, S. 2001, *ApJ*, 550, 897  
 Hurley, J. R., Tout, C. A., & Pols, O. R. 2002, *MNRAS*, 329, 897  
 Iben, I. Jr., Tutukov, A. V., & Yungelson, L. R. 1995, *ApJS*, 100, 233  
 In't Zand 2005, *A&A*, 441, L1  
 Kent, S. M., Dame, T. M., & Fazio, G. 1991, *ApJ*, 378, 131  
 King, A. R. 2000, *MNRAS*, 315, L33  
 King, A. R., Ricketts, M. J., & Warwick R. S. 1979, *MNRAS*, 187, 77  
 Krabbe, A. et al. 1995, *ApJ*, 447, L95  
 Kraft, R. P., Burrows, D. N., & Nousek, J. A. 1991, *ApJ*, 374, 344  
 Kong, A. K. H., McClintock, J. E., Garcia, M. R., Murray, S. S., & Barret, D. 2002, *ApJ*, 570, 277  
 Launhardt, R., Zylka, R., & Mezger, P. G. 2002, *A&A*, 384, 112  
 Law, C. & Yusef-Zadeh, F. 2004, *ApJ*, 611, 858  
 Laycock, S., Grindlay, J., van den Berg, M., Zhao, P., Hong, J., Koenig, X., Schlegel, E. M., & Persson, S. E. 2005, *ApJ* in press, astro-ph/0509783  
 Liu, Q. Z., van Paradijs, J., & van den Heuvel, E. P. J. 2001, *A&A*, 368, 1021  
 Liu, X. W. & Li X. D. 2005, astro-ph/0512019  
 Lu, F. J., Wang, Q. D., & Lang, C. C. 2003, *AJ*, 126, 319  
 Lyons, L. 1991, *A practical guide to data analysis for physical science students*, Cambridge University Press.  
 Manners, J. C. et al. 2003, *MNRAS*, 343, 293  
 Martí, J., Mirable, I. F., Chaty, S., & Rodríguez, L. F. 2000, *A&A*, 363, 184  
 McNamara, D. H., Madsen, J. B., Barnes, J., & Ericksen, B. F. 2000, *PASP*, 112, 202  
 Munro, M. P. et al. 2003a, *ApJ*, 589, 225  
 Munro, M. P. et al. 2004, *ApJ*, 613, 1179  
 Munro, M. P., Pfahl, E., Baganoff, F. K., Brandt, W. N., Ghez, A., Lu, J., & Morris, M. R. 2005a, *ApJ*, 622, L113  
 Munro, M. P., Bower, G. C., Burgasser, A. J., Baganoff, F. K., Morris, M. R., & Brandt, W. N. 2005, *ApJ* in press  
 Murdoch, H. S., Crawford, D. F., & Jauncey, D. 1973, *ApJ*, 183, 1  
 Patterson, J. 1984, *ApJS*, 54, 443  
 Pavlinsky, M. N., Grebenev, S. A., & Sunyaev, R. A. 1994, *ApJ*, 425, 110  
 Pfahl, E., Rappaport, S., & Podsiadlowski, P. 2002, *ApJ*, 571, L37  
 Pollock, A. M. T. 1987, *ApJ*, 320, 283  
 Porquet, D., Rodriguez, J., Corbel, S., Goldoni, P., Warwick, R. S., Goldwurm, A., & Decourchelle, A. 2003, *A&A*, 406, 299  
 Predehl, P. & Truemper, J. 1994, *A&A*, 290, L29  
 Robin, A. C., Reylé, C., Derrière, S. & Picaud, S. 2003, *A&A*, 409, 523  
 Ruiter, A. J., Belczynski, K., & Harrison, T. E. 2005, astro-ph/0511813  
 Sakano, M., Koyama, K., Murakami, H., Maeda, Y., & Yamauchi, S. 2002, *ApJS*, 138, 19  
 Sakano, M., Warwick, R. S., Decourchelle, A., & Wang, Q. D. 2005, *MNRAS*, 357, 1211  
 Sazonov, S., Revnivtsev, M., Gilfanov, M., Churazon, E., & Sunyaev, R. 2005, astro-ph/0510049  
 Sidoli, L., Belloni, T., & Mereghetti, S. 2001, *A&A*, 368, 835  
 Sidoli, L., Mereghetti, S., Israel, G. L., Chiappetti, L., Treves, A., & Orlandini, M. 1999, *ApJ*, 525, 215  
 Suleimanov, V., Revnivtsev, M., & Ritter, H. 2005, *A&A*, 435, 191  
 Takagi, S., Murakami, H., & Koyama, K. 2002, *ApJ*, 573, 275  
 Townsley, L. K. et al., 2002, *NIM-A*, 486, 751  
 Verbunt, F., Bunk, W. H., Ritter, H., & Pfeffermann, E. 1997, *A&A*, 327, 602  
 Wang, Q. D., Gotthelf, E. V., & Lang, C. C. 2002, *Nature*, 415, 148  
 Wang, Q. D. 2004, *ApJ*, 612, 159  
 Warner, B. 1995, *Cataclysmic Variable Stars*, Cambridge University Press  
 Watson, M. G., Willingale, R., Hertz, P., & Grindlay, J. E. 1981, *ApJ*, 250, 142  
 Weisskopf, M. C., Brinkman, B., Canizares, C., Garmire, G., Murray, S., & van Speybroeck, L. P. 2002, *PASP*, 114, 1  
 Wijnands, R., Guainazzi, M., van der Klis, M., & Méndez, M. 2002, *ApJ*, 573, L45  
 Wijnands, R., Miller, J. M., & Wang, Q. D. 2002, *ApJ*, 579, 422  
 Wijnands, R. & Wang, Q. D. 2002, *ApJ*, 568, L93  
 Wijnands, R. et al. 2005, *A&A* in press, astro-ph/0508648  
 Yusef-Zadeh, F., Law, C., Wardle, M., Wang, Q. D., Frusciione, A., Lang, C. C. & Cotera, A. 2002, *ApJ*, 570, 665  
 Yusef-Zadeh, F., Hewitt, J. W., Cotton, W. 2004, *ApJS*, 155, 421

TABLE B1  
 CATALOG OF POINT SOURCES WITHIN  $2^\circ \times 0.8^\circ$  OF THE GALACTIC CENTER

| Source<br>(CXO J) | ra<br>(J2000) | dec       | Unc.<br>(arcsec) | Obsid | Offset<br>(arcmin) | $T_{\text{exp}}$<br>(ks) | $C_{\text{net}}$       | $P_{\text{det}}$ | HR0                     | HR2                     | $F_X$ $10^{-7}$<br>(ph cm $^{-2}$ s $^{-1}$ ) | Flags |
|-------------------|---------------|-----------|------------------|-------|--------------------|--------------------------|------------------------|------------------|-------------------------|-------------------------|---|-------|
| 174204.8 – 295003 | 265.52017     | –29.83436 | 1.5              | 2289  | 11.3               | 11.6                     | $15.4^{+8.0}_{-6.9}$   | 0.00             | $-0.52^{+0.39}_{-0.42}$ | –9.00                   | 60.2  | sf    |
| 174206.8 – 293634 | 265.52844     | –29.60947 | 1.0              | 2290  | 6.4                | 11.6                     | $4.2^{+4.1}_{-2.7}$    | 0.25             | –9.00                   | $1.00_{-0.76}$          | 22.8  | ...   |
| 174208.5 – 294436 | 265.53574     | –29.74361 | 1.0              | 2290  | 6.5                | 11.6                     | $8.2^{+5.5}_{-4.0}$    | 0.27             | $-1.00^{+0.50}$         | –9.00                   | 24.8  | f     |
| 174210.4 – 293639 | 265.54358     | –29.61107 | 1.0              | 2290  | 5.7                | 11.6                     | $14.4^{+6.8}_{-5.0}$   | 0.95             | –9.00                   | $0.29^{+0.46}_{-0.45}$  | 64.7  | ...   |
| 174216.0 – 293756 | 265.56689     | –29.63249 | 0.9              | 2290  | 3.9                | 11.6                     | $8.7^{+5.0}_{-4.5}$    | 0.81             | $0.15^{+0.70}_{-0.73}$  | –9.00                   | 25.9  | ...   |
| 174216.1 – 293732 | 265.56723     | –29.62580 | 0.9              | 2290  | 4.2                | 11.6                     | $11.6^{+5.8}_{-5.3}$   | 0.99             | –9.00                   | $0.67^{+0.33}_{-0.34}$  | 57.0  | ...   |
| 174217.8 – 293715 | 265.57425     | –29.62091 | 0.9              | 2290  | 4.1                | 11.6                     | $10.6^{+5.6}_{-5.0}$   | 0.96             | $1.00_{-1.09}$          | $-0.35^{+0.58}_{-0.55}$ | 36.0  | ...   |
| 174218.6 – 293931 | 265.57761     | –29.65884 | 0.9              | 2290  | 2.7                | 11.6                     | $6.7^{+4.3}_{-4.0}$    | 0.94             | $1.00_{-1.09}$          | $0.20^{+0.80}_{-0.90}$  | 25.2  | ...   |
| 174219.2 – 294333 | 265.58029     | –29.72591 | 0.9              | 2290  | 4.1                | 11.6                     | $4.5^{+3.8}_{-3.0}$    | 0.17             | –9.00                   | $-1.00^{+0.74}$         | 14.1  | ...   |
| 174220.1 – 293526 | 265.58389     | –29.59068 | 0.9              | 2290  | 5.3                | 11.6                     | $4.5^{+3.9}_{-3.0}$    | 0.06             | $1.00_{-0.89}$          | –9.00                   | 13.5  | s     |
| 174220.1 – 293905 | 265.58414     | –29.65145 | 0.9              | 2289  | 2.6                | 11.6                     | $10.9^{+5.3}_{-5.3}$   | 0.99             | $-1.00^{+0.55}$         | $1.00_{-0.87}$          | 36.9  | f     |
| 174221.3 – 294250 | 265.58887     | –29.71409 | 0.9              | 2290  | 3.3                | 11.6                     | $2.7^{+2.7}_{-2.3}$    | 0.02             | –9.00                   | $-1.00^{+1.08}$         | 7.7   | ...   |
| 174221.3 – 294647 | 265.58902     | –29.77988 | 1.1              | 2286  | 6.9                | 11.6                     | $8.6^{+5.3}_{-4.8}$    | 0.63             | $1.00_{-1.13}$          | $0.46^{+0.55}_{-0.64}$  | 40.4  | ...   |
| 174222.8 – 294118 | 265.59518     | –29.68858 | 0.9              | 2290  | 2.0                | 11.6                     | $3.7^{+3.2}_{-2.8}$    | 0.34             | –9.00                   | $-0.00^{+0.99}_{-0.98}$ | 14.2  | ...   |
| 174223.3 – 293950 | 265.59735     | –29.66397 | 0.9              | 2290  | 1.7                | 11.6                     | $5.8^{+3.9}_{-3.7}$    | 0.69             | –9.00                   | $-0.35^{+0.77}_{-0.65}$ | 20.6  | ...   |
| 174224.2 – 293412 | 265.60095     | –29.57001 | 1.0              | 2290  | 6.2                | 23.2                     | $12.0^{+7.1}_{-5.3}$   | 0.53             | $1.00_{-0.85}$          | $-0.02^{+0.59}_{-0.56}$ | 29.7  | ...   |
| 174224.6 – 294333 | 265.60275     | –29.72592 | 0.9              | 2283  | 3.6                | 11.6                     | $8.6^{+5.1}_{-4.4}$    | 0.73             | $-0.01^{+0.99}_{-0.97}$ | $-1.00^{+0.64}$         | 22.3  | ...   |
| 174227.5 – 292602 | 265.61487     | –29.43403 | 1.2              | 2283  | 8.1                | 11.6                     | $66.5^{+13.9}_{-13.1}$ | 0.89             | $-0.55^{+0.18}_{-0.18}$ | $-0.20^{+0.76}_{-0.65}$ | 204.3   | sf    |
| 174228.3 – 294157 | 265.61816     | –29.69925 | 0.9              | 2290  | 1.8                | 23.2                     | $3.3^{+4.2}_{-3.0}$    | 0.11             | –9.00                   | $-0.12^{+1.13}_{-0.88}$ | 10.1  | ...   |
| 174228.4 – 293431 | 265.61850     | –29.57547 | 1.0              | 2290  | 5.7                | 23.2                     | $9.8^{+5.7}_{-5.4}$    | 0.09             | $-1.00^{+0.42}$         | $1.00_{-1.33}$          | 15.4  | f     |
| 174228.5 – 293736 | 265.61883     | –29.62687 | 0.9              | 2290  | 2.7                | 23.2                     | $7.8^{+5.8}_{-5.7}$    | 0.75             | –9.00                   | $1.00_{-1.13}$          | 20.3  | ...   |
| 174230.0 – 293949 | 265.62524     | –29.66380 | 0.9              | 2290  | 0.4                | 23.2                     | $4.3^{+5.1}_{-4.1}$    | 0.10             | –9.00                   | –9.00                   | 9.3   | ...   |
| 174230.3 – 294713 | 265.62646     | –29.78708 | 1.1              | 2283  | 7.0                | 11.6                     | $8.6^{+5.4}_{-4.7}$    | 0.17             | $1.00_{-0.92}$          | $-1.00^{+0.51}$         | 24.3  | ...   |
| 174230.6 – 294320 | 265.62769     | –29.72239 | 0.9              | 2290  | 3.1                | 23.2                     | $20.2^{+9.2}_{-7.7}$   | 0.99             | $0.07^{+0.62}_{-0.54}$  | $-1.00^{+0.98}$         | 46.9  | ...   |
| 174231.4 – 294336 | 265.63089     | –29.72681 | 0.9              | 2290  | 3.4                | 23.2                     | < 8.7                  | 0.00             | ...                     | ...                     | 8.9   | ...   |

NOTE. — The full table will be available online, and is on [http://astro.ucla.edu/munno/sgra/shallow\\_survey\\_catalog.txt](http://astro.ucla.edu/munno/sgra/shallow_survey_catalog.txt).